Molecular Monolayers for Electrical Passivation and Functionalization of Silicon-Based Solar Energy Devices

Janneke Veerbeek,[†] Nienke J. Firet,[†] Wouter Vijselaar,[†] Rick Elbersen,[†,‡] Han Gardeniers,[‡] and Jurriaan Huskens*[†]

[†]Molecular NanoFabrication and [‡]Mesoscale Chemical Systems groups, MESA+ Institute for Nanotechnology, University of Twente, P.O. Box 217, 7500 AE Enschede, The Netherlands

S *Supporting Information*

ABSTRACT: Silicon-based solar fuel devices require passivation for optimal performance yet at the same time need functionalization with (photo)catalysts for efficient solar fuel production. Here, we use molecular monolayers to enable electrical passivation and simultaneous functionalization of silicon-based solar cells. Organic monolayers were coupled to silicon surfaces by hydrosilylation in order to avoid an insulating silicon oxide layer at the surface. Monolayers of 1-tetradecyne were shown to passivate silicon micropillar-based solar cells with radial junctions, by which the efficiency increased from 8.7% to 9.9% for n^+/p junctions and from 7.8% to 8.8% for p^+/n junctions. This electrical passivation of the surface, most likely by removal of dangling bonds, is reflected in a higher shunt resistance in the $J-V$ measurements. Monolayers of 1,8-nonadiyne were still reactive for click chemistry with a model catalyst, thus enabling simultaneous passivation and future catalyst coupling.

KEYWORDS: *silicon solar cells, organic monolayers, electrical passivation, shunt resistance, hydrosilylation*
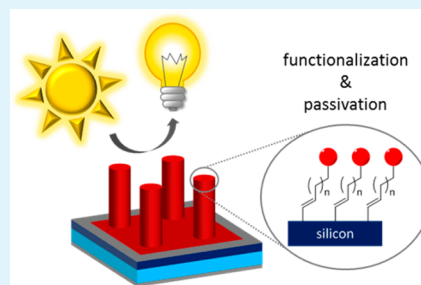
INTRODUCTION

Silicon solar cells have gained increasing attention for electricity production, due to silicon's ease of fabrication, wide availability, and charge separation by using a p/n junction.[1−3] Due to the intermittent presence of sunlight, however, a steady power output is not feasible by photovoltaic cells only. Therefore, it is much more attractive to use sunlight to produce solar fuels, in which solar energy can be stored until needed.[4,5] Examples of solar fuels include hydrogen from water splitting[6,7] or carbon-based fuels, such as CO, CH_4, or CH_3OH, from water splitting and CO_2.[8] One of the envisioned solar-to-fuel devices consists of a tandem configuration, containing two semiconductors assembled with a membrane in between and catalysts on each side to assist water splitting.[9,10] In this way, the solar cell converts sunlight into power, the catalysts use this power output to split water, and the evolved gases are kept separate by the membrane. To obtain the most efficient, integrated solar-to-fuel device, both an efficient solar cell and catalysts coupled to the surface are required. We focus here on devices that use silicon as one of the semiconductors, primarily for the hydrogen production side.

Structuring of silicon solar cells can increase the solar cell output by a higher surface area for light absorption and less reflection, e.g., using micropyramids or nano/micropillars with radial junctions.[11−13] Nano/microstructuring increases the surface area but inevitably also the amount of dangling bonds at the surface. This constitutes undesired recombination sites for electron−hole pairs, thus lowering the output of the solar cell. The negative effect of dangling bonds can be suppressed by applying an electrical passivation layer,[14−16] e.g., an inorganic layer of silicon oxide, silicon nitride, or aluminum oxide.[11,16−18]

A solar-to-fuel device requires catalyst functionalization and passivation at the same time. For catalyst coupling to silicon, numerous literature examples have shown hydrogen production.[10,18−21] In such an architecture, combining passivation and catalyst coupling can only be obtained in two steps, i.e., first catalyst deposition and then selectively applying a passivation layer via a bottom-up method that does not overgrow the catalyst[22] or vice versa.[18] Molecular monolayers, however, offer the solution to fulfill both surface passivation and subsequent catalyst coupling. Monolayer-forming adsorbates can be bound to silicon by direct Si−C bonds in order to avoid the presence of silicon oxide as insulating layer and function as an electrical passivation layer.[23−27] A few articles have reported the combination of passivation and secondary functionalization,[28−30] but to our knowledge, this method has not been applied to silicon solar cells yet.

Here, we use organic molecular monolayers for electrical passivation and simultaneous functionalization of silicon solar cells. Covalent monolayer coupling has been achieved by hydrosilylation, which is a one-step reaction in which molecules with unsaturated carbon−carbon end groups are coupled to hydrogen-terminated silicon.[31,32] 1-Tetradecyne has been used to study the passivation effect on silicon solar cells by $J-V$ measurements. Silicon solar cells have been fabricated with

Scheme 1. Schematic Representation of Monolayer Coupling to Planar and Radial Junctions at Planar and Pillared Si Substrates, Respectively, By Hydrosilylation. Aluminum Contacts Are Created in Order to Assess the Solar Cell Properties of the Substrates
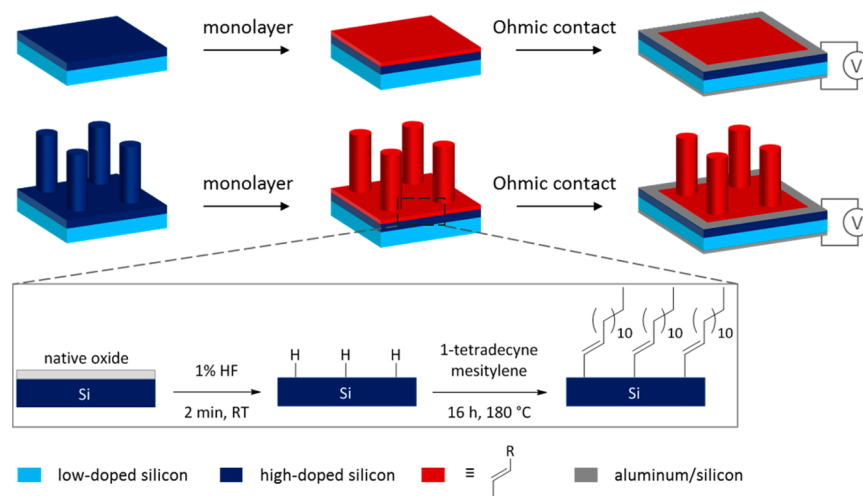
Table 1. Static Water Contact Angle Values before and after Monolayer Formation

	1% HF	control	1-tetradecyne	1,8-nonadiyne
n^+/p planar	$42.3° \pm 0.8$	$94.1° \pm 1.1$	$108.0° \pm 2.6$	$76.0° \pm 2.3$
n^+/p radial		$91.4° \pm 0.5$	$108.5° \pm 0.4$	
p^+/n planar	$43.6° \pm 2.3$	$87.1° \pm 2.7$	$98.0° \pm 0.5$	$82.6° \pm 2.0$
p^+/n radial		$84.8° \pm 2.3$	$95.4° \pm 0.8$	

planar junctions in 2D and radial junctions in 3D micropillars in order to assess the effect of Si microstructuring on the passivation effect. To test the versatility of this platform, the passivation effect was investigated on both n^+/p and p^+/n junctions. A monolayer of the dialkyne 1,8-nonadiyne has been studied to demonstrate that the passivation layers are still available for further functionalization. As a proof of concept, a fluorescent dye has been coupled as model catalyst by the well-developed click chemistry.[33]

RESULTS AND DISCUSSION

Monolayer Passivation. Silicon solar cells with a junction were fabricated in 2D substrates and 3D micropillars (4 μm diameter, 6 μm pitch, about 40 μm length, Figure S1). Planar and pillared Si substrates were doped to create planar and radial junctions, respectively, according to a procedure reported before.[34] Both n^+/p junctions (defined as p-type base with phosphorus doping) and p^+/n junctions (n-type base wafers doped with boron) were created, with a junction depth of approximately 1 μm.

In order to passivate the surface, monolayers were coupled to these substrates by a thermal hydrosilylation method in which chemical compounds with unsaturated end groups are grafted onto oxide-free silicon (Scheme 1).[31,35] To that purpose, the silicon substrates were immersed in an aqueous 1% hydrofluoric acid (HF) solution to remove the native oxide layer and create a hydrogen-terminated surface. An alkyne-terminated molecule, i.e., 1-tetradecyne with a methyl end group, was coupled to hydrogen-terminated silicon to create a Si−C≡C−R monolayer. This molecule was chosen because of its hydrophobic nature, enabling easy proof of monolayer presence by contact angle measurements.

The contact angle of hydrogen-terminated silicon was 42−44° (Table 1) and increased upon hydrosilylation with 1-tetradecyne to ∼108° for n^+/p junctions and ∼95−98° for p^+/n junctions, as measured on the planar substrates or planar regions next to the pillar arrays. These values are characteristic for hydrophobic surfaces, thus indicating that the monolayer coupling was successful. The large difference in contact angle between n^+ and p^+ surfaces has been reported before for a visible light-induced hydrosilylation reaction[36] and was attributed to the formation of more electron−hole pairs in n^+ substrates, which speeds up the radical chain mechanism. The control samples without a monolayer were processed through all steps, but their hydrosilylation step was mimicked with solvent only. For these control samples, the contact angle was ∼91−94° for n^+/p junctions and ∼84−87° for p^+/n junctions, which is (inexplicably) higher than the values of the hydrogen-terminated samples.

Attenuated total reflection infrared spectroscopy (ATR-IR) spectra of dummy substrates, functionalized simultaneously with the solar cell samples, confirmed the presence of a 1-tetradecyne monolayer by disappearance of the Si−H_x stretching modes at 2112 cm^{-1} and the appearance of CH_3, CH_2 (antisymmetric), and CH_2 (symmetric) peaks at 2961, 2922, and 2853 cm^{-1}, respectively (Figure 1). As expected, no peaks appeared in the spectra of the control samples, thus indicating that no monolayer was formed on these bare samples.

In order to characterize the substrates as solar cells, Ohmic contacts of an aluminum/silicon alloy were fabricated at the front and back side. The presence of a monolayer at the interface between the solar cell interface and the metal contact suppressed the conductance significantly, probably due to a poor contact between the aluminum and the silicon (data not shown). Therefore, to fabricate an Ohmic contact at the front
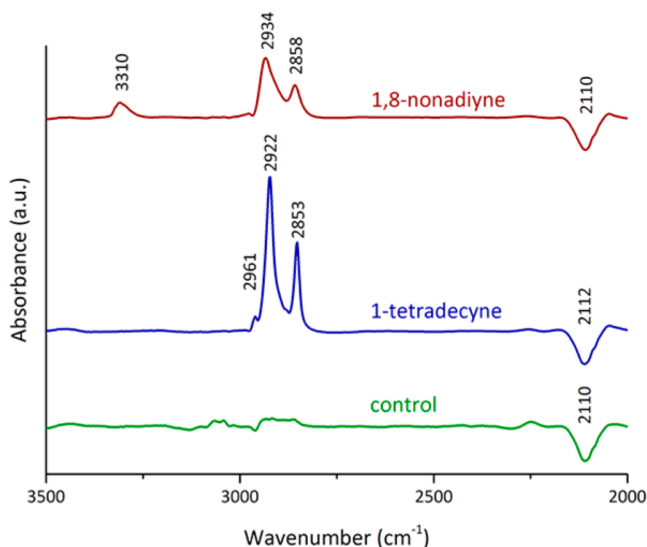
Figure 1. ATR-IR spectra of silicon substrates without functionalization (control) and functionalized with 1-tetradecyne or 1,8-nonadiyne, all referenced to a H-terminated silicon sample.

side of the samples, the active solar cell area (0.5×0.5 cm^2) was first protected by photoresist masking. The 1-tetradecyne monolayer was then selectively removed outside the active solar

cell areas by oxygen plasma, followed by removal of the resist. The thin silicon oxide layer induced by the oxygen plasma treatment was removed in 1% HF. The monolayers on the active solar cell areas were still intact after this treatment, as indicated by the high hydrophobicity on the planar junctions. Hereafter, aluminum/silicon alloy was sputtered outside the solar cell areas and on the back side of the samples.

$J-V$ measurements were performed to investigate the effect of the monolayers on the solar cell performance. The efficiency (η) of a solar cell can be calculated by eq 1

$$\eta = \frac{V_{oc}J_{sc}FF}{P_{in}} \tag{1}$$

where V_{oc} is the open-circuit voltage, J_{sc} is the short-circuit current density, FF is the fill factor, and P_{in} is the input power (100 mW/cm^2, AM 1.5G). An ideal solar cell would show rectangular $J-V$ behavior, with V_{oc}, J_{sc}, and FF as high as possible. FF mainly depends on two resistances, i.e., the shunt resistance (R_{sh}) and the series resistance (R_s). R_{sh} equals the inverse slope of the $J-V$ curve at J_{sc}, which becomes higher when there are less leaking pathways for the current as is achieved by more effective surface passivation.[37,38] R_s equals the inverse slope of the $J-V$ curve at V_{oc} and reflects the resistance in the materials through which the current passes, and R_s should be as low as possible.
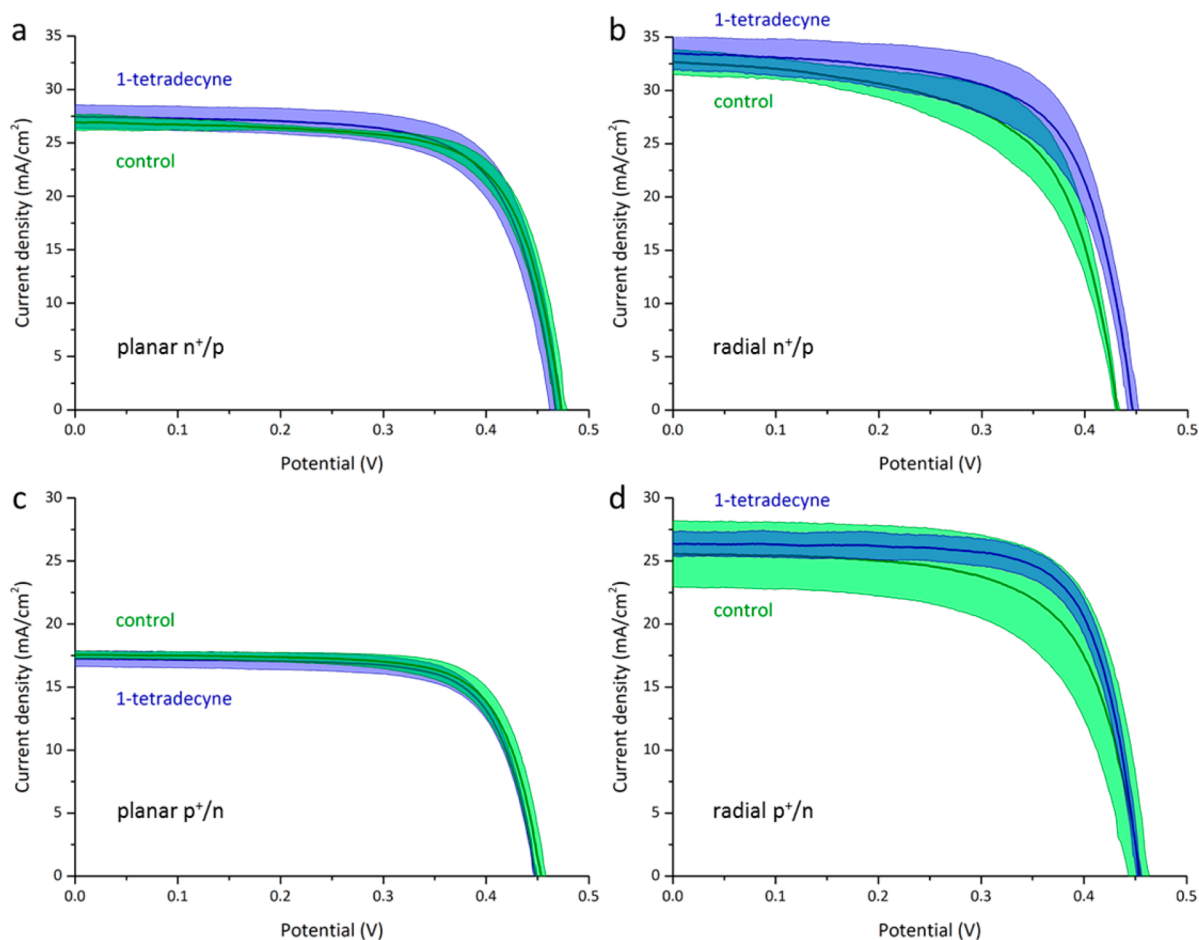
Figure 2. $J-V$ measurements of Si samples with (a) planar and (b) radial n$^+$/p junctions (p-type base wafer) and (c) planar and (d) radial p$^+$/n junctions (n-type base wafer) with and without a 1-tetradecyne monolayer. Shaded areas indicate the 1σ range around the average (at least four samples were analyzed for each configuration).

**Table 2. J−V Characteristics of n⁺/p Planar and Radial Junctions with and without a 1-Tetradecyne Monolayer**

	planar p⁺/n junctions			radial p⁺/n junctions		
	control	1-tetradecyne	±	control	1-tetradecyne	±
R_s ($\Omega\cdot cm^2$)	1.5 ± 0.1	1.5 ± 0.1	−2%[a]	1.6 ± 0.1	1.5 ± 0.1	9%[a]
R_{sh} ($k\Omega\cdot cm^2$)	0.61 ± 0.59	0.69 ± 0.02	15%	0.21 ± 0.03	0.32 ± 0.08	57%
V_{oc} (V)	0.47 ± 0.01	0.47 ± 0.01	−1%	0.43 ± 0.01	0.45 ± 0.01	4%
J_{sc} (mA/cm^2)	26.9 ± 0.8	27.4 ± 1.1	2%	32.7 ± 1.2	33.5 ± 1.5	2%
FF (%)	71 ± 4	70 ± 2	−1%	62 ± 8	66 ± 4	7%
η (%)	9.0 ± 0.4	9.0 ± 0.6	0%	8.7 ± 1.0	9.9 ± 1.1	14%

[a] R_s should be as low as possible, so a lower value is shown as positive difference

Table 3. J−V Characteristics of p⁺/n Planar and Radial Junctions with and without a 1-Tetradecyne Monolayer

	planar p⁺/n junctions			radial p⁺/n junctions		
	control	1-tetradecyne	±	control	1-tetradecyne	±
R_s ($\Omega\cdot cm^2$)	2.2 ± 0.1	2.3 ± 0.1	−2%[a]	1.9 ± 0.3	1.5 ± 0.1	27%[a]
R_{sh} ($k\Omega\cdot cm^2$)	1.4 ± 0.2	1.4 ± 0.2	4%	0.91 ± 0.11	1.6 ± 0.1	74%
V_{oc} (V)	0.45 ± 0.01	0.45 ± 0.01	−1%	0.45 ± 0.01	0.45 ± 0.01	0%
J_{sc} (mA/cm^2)	17.6 ± 0.3	17.3 ± 0.6	−2%	25.6 ± 2.6	26.4 ± 1.0	3%
FF (%)	74 ± 3	74 ± 1	0%	67 ± 6	73 ± 1	9%
η (%)	5.9 ± 0.3	5.7 ± 0.3	−3%	7.8 ± 1.5	8.8 ± 0.4	12%

[a] R_s should be as low as possible, so a lower value is shown as positive difference
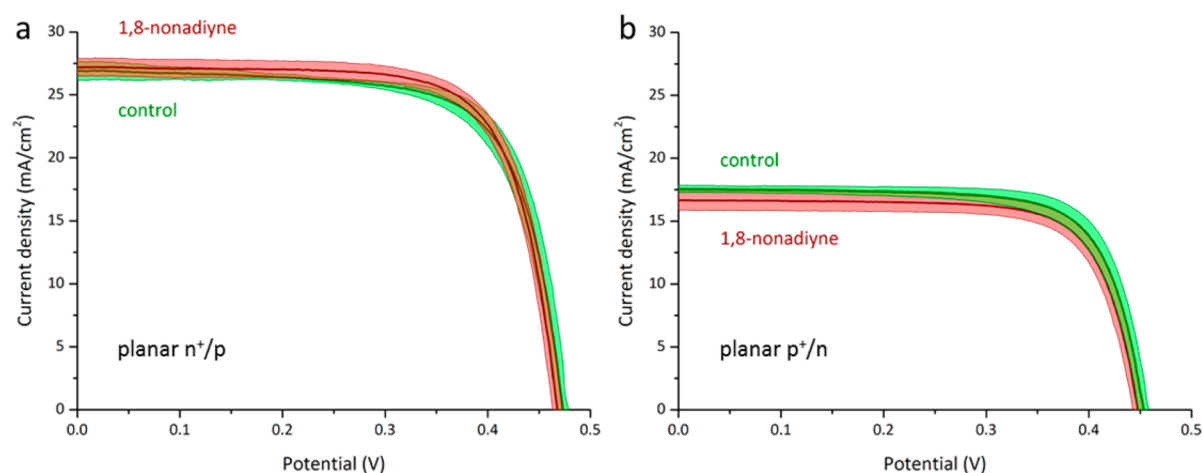
Figure 3. J−V measurements of planar (a) n⁺/p junctions (p-type base wafer) and (b) p⁺/n junctions (n-type base wafer) with and without a 1,8-nonadiyne monolayer. Shaded areas indicate the 1σ range around the average (at least four samples were analyzed for each configuration).

J−V measurements were performed on both planar and micropillar array samples with n⁺/p and p⁺/n junctions (Figure 2). The overall performance of planar n⁺/p (Figure 2a, Table 2) and p⁺/n junctions (Figure 2c, Table 3) did not change significantly after functionalization with a 1-tetradecyne monolayer. Internally, however, R_{sh} increased by 15% and 4%, respectively, thus indicating the expected positive effect of surface passivation. The J−V response for micropillar arrays with radial n⁺/p (Figure 2b, Table 2) and p⁺/n junctions (Figure 2d, Table 3) did improve significantly. Adding a monolayer enhanced all characteristic parameters, so that the efficiency increased from 8.7% to 9.9% for n⁺/p junctions and from 7.8% to 8.8% for p⁺/n junctions. Notably, R_{sh} increased from 0.21 to 0.32 kΩ·cm² (57% increase) for n⁺/p junctions and from 0.91 to 1.6 kΩ·cm² (74% increase) for p⁺/n junctions, thus confirming surface passivation by the monolayer. The improved efficiencies mainly originate from these differences in R_{sh}, whereas the V_{oc} and J_{sc} values changed only slightly, which

shows that this passivation method results in an intrinsic change in material properties.

The passivation effect can also be derived from plotting the local ideality factor versus the potential (Figure S2), as extracted from the J−V behavior in the dark. The local ideality factor is expected to decrease when the number of defect sites is lowered upon applying a passivation layer.[39,40] This effect was indeed observed for n⁺/p junctions, where the local ideality factor decreased for both planar and micropillar array samples with a 1-tetradecyne monolayer compared to unfunctionalized samples. For p⁺/n junctions, no difference in local ideality factor was observed, but the more pronounced differences in R_{sh} already confirmed the passivation effect on these junctions.

The passivation effect is most clearly visible on the micropillared solar cells, which can be explained by the difference in absolute surface area compared to a planar solar cell. With the micropillar layout used the total surface area has increased by a factor of ~17. As stated before, dangling bonds at the silicon surface provide undesired recombination sites for

Table 4. J−V Characteristics of Planar n⁺/p and p⁺/n Junctions with and without a 1,8-Nonadiyne Monolayer

	planar n⁺/p junctions			planar p⁺/n junctions		
	control	1,8-nonadiyne	±	control	1,8-nonadiyne	±
R_s ($\Omega \cdot cm^2$)	1.5 ± 0.1	1.5 ± 0.1	4%[a]	2.2 ± 0.1	2.3 ± 0.1	−6%[a]
R_{sh} ($k\Omega \cdot cm^2$)	0.61 ± 0.59	1.74 ± 0.01	188%	1.4 ± 0.2	1.6 ± 0.1	19%
V_{oc} (V)	0.47 ± 0.01	0.47 ± 0.01	−1%	0.45 ± 0.01	0.45 ± 0.01	−1%
J_{sc} (mA/cm^2)	26.9 ± 0.8	27.2 ± 0.7	1%	17.6 ± 0.3	16.7 ± 0.8	−5%
FF (%)	71 ± 4	73 ± 1	3%	74 ± 3	74 ± 1	1%
η (%)	9.0 ± 0.4	9.3 ± 0.2	3%	5.9 ± 0.3	5.5 ± 0.3	−5%

[a]R_s should be as low as possible, so a lower value is shown as positive difference
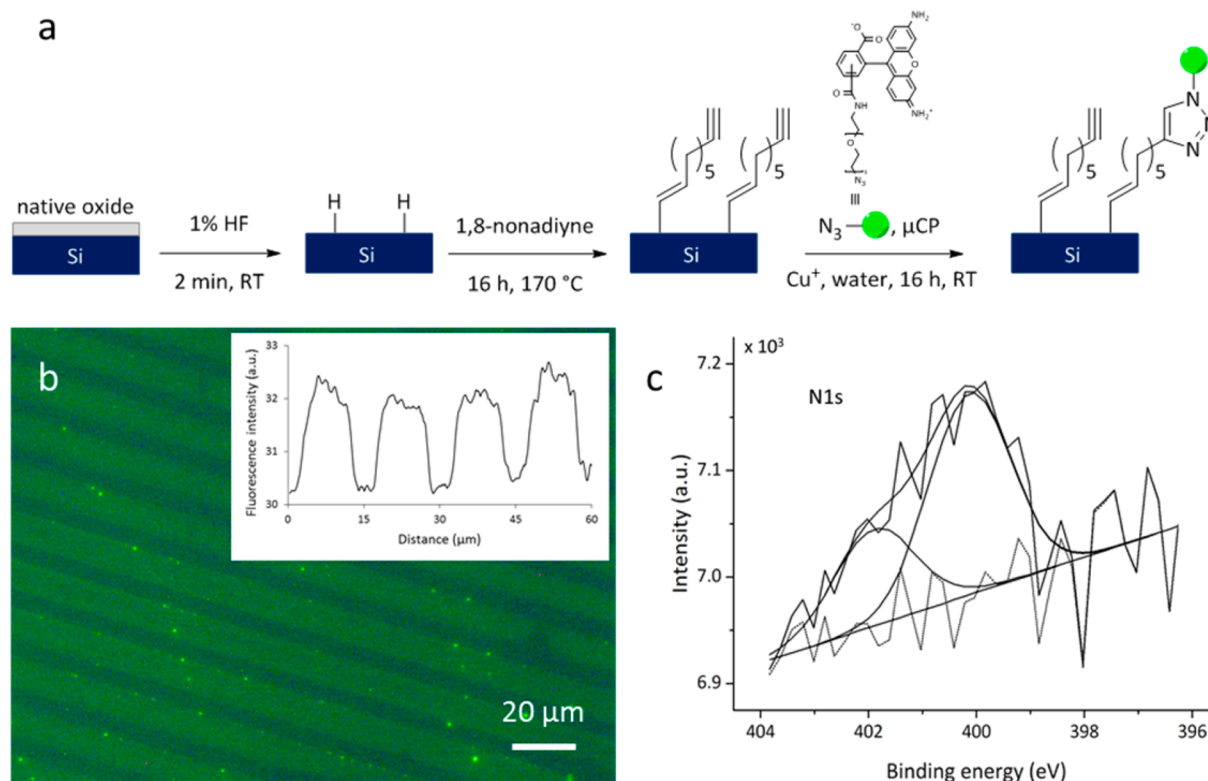
Figure 4. (a) Schematic representation of 1,8-nonadiyne coupling to silicon by hydrosilylation and subsequent click chemistry with an azide-functionalized dye, (b) fluorescence microscopy image after microcontact printing, exposure time 10 s, brightness increased by 30% (inset shows fluorescence intensity profile of the original image), and (c) XPS spectrum of the N 1s region after microcontact printing, including deconvoluted signals.

electron−hole pairs, which can be suppressed by coupling a molecular monolayer onto the surface. The micropillar solar cells contain more dangling bonds due to both their 3D structuring and the introduction of scallops during the pillar fabrication.[11,41] This makes the effect of a molecular passivation layer more pronounced, thus making the need for passivation more evident.

Dual Passivation and Functionalization. To allow both passivation and functionalization, an adsorbate with two functional groups, at the head and tail of the molecule, is required. A suitable choice is the dialkyne 1,8-nonadiyne, where one alkyne group can be coupled to the solar cell by hydrosilylation and the other alkyne group can be functionalized subsequently with an azide-containing molecule using the well-studied copper-catalyzed click chemistry[33] or thiol−yne chemistry.[42]

Because we expected a very similar passivation effect of 1,8-nonadiyne compared to 1-tetradecyne, the electrical passivation effect of 1,8-nonadiyne was tested only on planar silicon solar cells. The hydrosilylation reaction was carried out in pure 1,8-nonadiyne in order to suppress back bending of the second alkyne group toward the hydrogen-terminated silicon surface. The contact angle of 1,8-nonadiyne-terminated surfaces was 76.0° and 82.6° for n⁺/p and p⁺/n planar junctions, respectively (Table 1). The latter value is similar to the literature, where 82° was reported for a 1,8-nonadiyne monolayer on p⁺ silicon.[43] ATR-IR further evidenced the monolayer formation by the disappearance of Si−H$_x$ stretching modes at 2110 cm⁻¹ and the appearance of C≡CH, CH₂ (antisymmetric), and CH₂ (symmetric) peaks at 3310, 2934, and 2858 cm⁻¹, respectively (Figure 1), similar to spectra reported in the literature.[42]

After aluminum/silicon contact formation, J−V measurements on the planar junctions did not show a significant difference of the efficiencies (Figure 3, Table 4). Looking at the individual parameters, however, R_{sh} was improved, which indicates a passivated surface. The largest increase was observed for n⁺/p junctions (Figure 3a), similarly as described above for 1-tetradecyne. The values of R_{sh} for the 1,8-nonadiyne-

Scheme 2. Schematic Fabrication Process with (a) Micropillar Fabrication Using Deep Reactive Ion Etching, (b) Radial Junction Formation by Dopant Deposition and in-Diffusion, Followed by Silicon Nitride Removal, (c) Organic Monolayer Coupling by Hydrosilylation, (d) Photoresist Coverage and Photolithography, (e) Monolayer Removal Outside the Active Solar Cell Areas and Ohmic Contact Formation at the Front and Back Sides
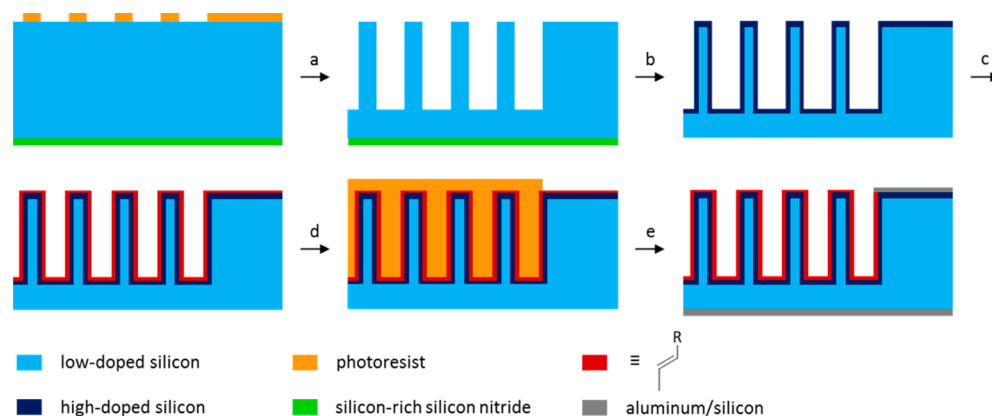
functionalized samples were higher than those obtained with 1-tetradecyne, indicating a better electrical passivation effect. This trend was also observed by a decrease of the local ideality factor (Figure S2), which was for planar n^+/p junctions even close to ideal diode behavior, as featured by a local ideality factor below 2 under forward bias.[39]

As a proof of concept to confirm that the alkyne headgroup is still available for further functionalization, click chemistry was performed with an azide-functionalized dye as a model catalyst (Figure 4a). Microcontact printing was used to provide contrast with the background signal in fluorescence microscopy. A planar silicon substrate was successfully functionalized with azide-fluor 488 (Figure 4b). A line pattern is observed with a periodicity equal to that of the stamp used. X-ray photoelectron spectroscopy (XPS) of the monolayer after click chemistry showed the presence of the triazole moiety by two characteristic bands at 400 and 402 eV in the N 1s region (Figure 4c) in the expected 2:1 ratio. Any physisorbed azide species would have appeared at 405 eV,[33] which was not observed in this spectrum (data not shown). Further evidence for the formation of the dye monolayer is the appearance of a peak at 288 eV in the C 1s spectrum owing to the introduction of carbonyl groups (Figure S3).

CONCLUSIONS

In summary, we have shown the electrical passivation of silicon solar cells using molecular monolayers of 1-tetradecyne and 1,8-nonadiyne. The passivation effect was particularly observed by a substantial increase of the shunt resistance, which increased by 57% and 74% for n^+/p and p^+/n micropillar solar cells, respectively, when adding a monolayer of 1-tetradecyne. The molecular monolayers suppressed dangling bonds at the silicon surface, thus preventing recombination at those sites. This passivation effect was less pronounced in the case of planar junctions, because of their lower surface area and thus lower number of dangling bonds. Nevertheless, an increasing trend in shunt resistance was observed from control samples toward samples with monolayers of 1-tetradecyne and 1,8-nonadiyne. The latter monolayer was still available for further functionalization, as shown by coupling to a model catalyst. Since the length of the nonadiyne is less than 1 nm, we expect still a decent electrical contact between silicon and any catalyst bound on top of the monolayer, as indicated by the use of alkyl

monolayers to prepare molecular junctions[44,45] and the successful detection of redox-active groups on silicon bridged through alkyl monolayers.[46,47] In the same manner, it should therefore be possible to functionalize silicon solar cells with an azide-functionalized photocatalyst toward a solar-to-fuel device. The resistance of the monolayer could be lowered by the use of conjugated molecules as passivation and functionalization layer.[48,49]

MATERIALS AND METHODS

Materials. Silicon wafers (⟨100⟩ oriented, 100 mm diameter, single side polished) were obtained from Okmetic (Finland) as p-type (boron, resistivity 5−10 Ω·cm, thickness 525 μm) or n-type (phosphorus, 1−10 Ω·cm, 375 μm). For infrared spectroscopy, double-sided p-type silicon wafers were used with parameters equal to the single-side-polished p-type wafers. Mesitylene (>98%, Sigma-Aldrich) and 1,8-nonadiyne (98%, Sigma-Aldrich) were dried over molecular sieves (0.3 nm). Acetone (VLSI, BASF), acetonitrile (ACS grade, CH_3CN, Merck), azide-fluor 488 (>90%, Sigma-Aldrich), buffered hydrogen fluoride (VLSI, BHF, 7:1, Technic France), dichloromethane (99.7%, Actu-All), ethanol (absolute, VWR), ethylenediaminetetraacetic acid disodium salt dihydrate (>99%, EDTA, Sigma-Aldrich), hydrofluoric acid 1% (aqueous, VLSI, Technic France), phosphate-buffered saline powder (pH 7.4, results in 10 mM PBS with 0.138 M NaCl, Sigma-Aldrich), photoresist AZ9260 (Merck Microchemicals), photoresist OiR 906-12 (Fujifilm), 2-propanol (VLSI, BASF), resist developer OPD 4262 (Fujifilm), 1-tetradecyne (>97%, Sigma-Aldrich), tetrakis(acetonitrile)copper(I) hexafluorophosphate (Cu(I) $(CH_3CN)_4PF_6$, Sigma-Aldrich), and Tween-20 (Aldrich) were used as received. Tris-(benzyltriazolylmethyl)amine (TBTA) was synthesized according to a procedure from the literature.[50] Hexane was obtained from a solvent purification system (MB SPS-800). Milli-Q water with a resistivity > 18 MΩ·cm was obtained from a Milli-Q Integral water purification system (Merck Millipore). Glassware used for the hydrosilylation reactions was dried overnight at 120 °C.

Fabrication of Silicon Micropillars. Silicon micropillars were fabricated as reported before[34] but without the use of silicon dioxide as a hard mask (Scheme 2). In short, cleaned silicon substrates were covered with a 100 nm thick silicon-rich silicon nitride layer (SiRN) using low-pressure chemical vapor deposition (LPCVD). The SiRN layer was removed from the front side using reactive ion etching, leaving a protective SiRN layer at the back side. After cleaning, a photoresist layer (OiR 906-12) on the front side was patterned by standard photolithography, resulting in 0.5 × 0.5 cm² hexagonal arrays of dots (diameter 4 μm, spacing 2 μm, packing density 35%) for each 2 × 2 cm² sample. This resist layer functioned as a mask during deep

reactive ion etching of silicon using the Bosch process. This process resulted in micropillars with a length of approximately 40 μm, which were cleaned by an O_2/CF_4 plasma before further processing.

Junction Fabrication. Planar silicon substrates and the silicon micropillars fabricated as described above were doped as reported before.[34] Doping was performed on freshly cleaned substrates by depositing a dopant containing oxide layer, followed by a thermal drive-in step to diffuse the dopant into the silicon. In the case of n$^+$/p junctions, p-type substrates were covered with a phosphorus oxide layer by LPCVD. Thermal diffusion was performed at 1050 °C for 15 min under nitrogen flow. Opposite p$^+$/n junctions were created by doping n-type substrates with boron by solid-source dotation (SSD). A boron oxide (B_2O_5) layer was grown from boron nitride source wafers and simultaneously diffused into the silicon at 1050 °C for 15 min. After removal of the remaining B_2O_5 layer by 10 min immersion in BHF, the wafers were further oxidized at 800 °C for 30 min to remove the Si−B bonds. The back side of these wafers was doped with phosphorus (similarly as described above) to create n$^+$ Si, which was needed to create Ohmic contacts later on. In all cases, the SiRN protection layer was removed, and the samples were cleaned before further processing.

Monolayer Coupling. To couple the alkyne-terminated molecules to the silicon substrates, first a hydrogen-terminated surface was created by 2 min immersion in an aqueous 1% HF solution. Subsequently, the wafers were transferred into a full-wafer setup, equipped with a capillary as nitrogen inlet and a reflux condenser, which was flushed with nitrogen for 10 min. The adsorbate solution (80 mL), consisting of a 5% v/v solution of 1-tetradecyne in mesitylene or pure 1,8-nonadiyne, was added to the setup via a septum after degassing the solution by four freeze−pump−thaw cycles. The control samples were processed through the same steps as the samples with a monolayer, but the reaction step was performed in pure mesitylene, i.e., in the absence of adsorbate. The hydrosilylation reactions were performed overnight under continuous nitrogen flow at 180 °C for 1-tetradecyne, 170 °C for 1,8-nonadiyne, and 180 °C for the control samples in pure mesitylene. The wafers were cleaned by immersion in hexane, rinsing with ethanol, 10 min ultrasonication in dichloromethane to remove any physisorbed material, and subsequently dried in a stream of nitrogen. The functionalized samples were sealed in a nitrogen glovebox and stored under nitrogen prior to characterization.

The monolayer was removed outside the active solar cell areas in order to make a proper Ohmic contact. Therefore, the active areas were first protected with photoresist. The planar junctions were protected by spin coating photoresist (OiR 906-12, 6000 rpm, 30 s) on top of the monolayer. The resist layer was baked at 95 °C for 90 s, patterned using standard photolithography (3 s UV exposure), and immersed in resist developer (OPD 4262, 45 s). The micropillar arrays were protected by spin coating photoresist (AZ9260, 1000 rpm, 30 s) in between the pillars, overnight drying in a desiccator at 1×10^{-3} mbar, photolithography (3 cycles of 10 s UV exposure and 10 s delay), and resist development (OPD 4262, 7 min). In all cases, the wafers were exposed to oxygen plasma (Tepla 300E, 0.25 mbar, 300 W) for 2 min to remove the monolayer from the nonactive areas. On the planar junctions, the solar cell area was marked before resist removal in order to align the Ohmic contacts later on. The resist was removed by 15 min ultrasonication in acetone. Afterward, the samples were rinsed with 2-propanol and dried under nitrogen.

Click Chemistry by Microcontact Printing. Poly-(dimethylsiloxane) (PDMS) stamps were prepared by casting the precursor and curing agent (Sylgard 184, Dow Corning) at a 10:1 volume ratio onto a silicon master. Air bubbles were removed by vacuum for 30 min, and the stamps were cured overnight at 60 °C. Before microcontact printing, the cut stamps (10 μm lines and 5 μm spacing) were oxidized by oxygen plasma (power tuned to 40 mA) for 30 s. The stamps were inked with 75 μL of azide-fluor 488 solution (2 mM in CH_3CN) and 25 μL of catalyst solution (2 mM Cu(I)-(CH_3CN)$_4$PF$_6$ and 2 mM TBTA in CH_3CN/EtOH, ratio 2:1 v/v) for 4 min. After drying in a stream of nitrogen, the stamp was brought into conformal contact with a planar substrate (functionalized with a monolayer of 1,8-nonadiyne) for 2 h. Subsequently, the printed substrate was rinsed with acetonitrile and ethanol and sonicated in PBS with 0.05% v/v Tween-20 for 1 min. After rinsing with a 0.05% w/v EDTA solution in water to remove any copper traces, the substrate was dried under nitrogen.

Contact Angle Measurements. Static contact angles were measured with Milli-Q water droplets on a Krüss G10 Contact Angle Measuring Instrument equipped with a CCD camera. Contact angle values were determined automatically by a drop shape analysis software. Contact angles were measured immediately after the hydrosilylation. At least three drops were measured and averaged. On the micropillar arrays, the contact angle was measured on the planar regions next to the pillars.

Attenuated Total Reflection Infrared Spectroscopy. Infrared spectra were measured on double-side-polished silicon wafer pieces treated similarly to the solar cell samples. Spectra were collected with a Bruker spectrometer (Vertex 70v) equipped with an attenuated total reflection accessory ($L = 15$ mm) and MCT detector. The spectra were recorded with a resolution of 4 cm^{-1} and 1024 scans. Each spectrum was referenced to a hydrogen-terminated silicon sample. A spline baseline correction was applied.

J−V Measurements. Ohmic contacts were made in order to study the electrical properties of the formed junctions by recording J−V curves. Native oxide was removed from the wafers by a 1% HF dip, followed by sputtering a 1 μm thick layer of aluminum/silicon alloy (99/1% Al/Si, Oxford PL400, 500 W, 8:24 min) at the front side and 500 nm at the back side. At the front side, the active solar cell areas were protected by a stainless steel mask. The wafers were diced into single solar cells with 0.5×0.5 cm^2 active area and surrounding aluminum up to 2×2 cm^2. Samples were positioned perpendicular to a 300 W xenon arc light source with a filter. The position of the samples with respect to the lamp was calibrated to 1 sun intensity (AM 1.5G). J−V curves were recorded with a VersaSTAT 4 potentiostat from −0.7 to 0.7 V at 0.2 V/s. For each setting at least four different samples were measured and averaged. The current densities were normalized to the sample area, instead of the actual surface area of the pillars. The series and shunt resistances were determined by linearly fitting the inverse slope of the average graph at the x axis ($-10 < J < 10$ mA/cm^2) and y axis ($-0.15 < V < 0.15$), respectively. The minimum and maximum series and shunt resistance were acquired by fitting the average graph ± standard deviation, after which the standard deviation of the resistances was determined by one-fourth of the range.

The local ideality factor was extracted from the dark J−V measurements by determining the slope of the ln(J) versus potential plot for each potential value according to eq 2 and then averaging the local ideality factor over five points. The relation between current density (in the dark) and potential is given by the Shockley diode equation

$$\ln(J) = \ln(J_0) + \left(\frac{q}{nkT}\right)V \tag{2}$$

where J is the current density, J_0 is the dark saturation current density, q is the absolute value of electron charge, n is the ideality factor, k is the Boltzmann constant, T is the absolute temperature, and V is the potential.

High-Resolution Scanning Electron Microscopy (HR-SEM). HR-SEM images of cross sections of micropillar arrays were taken with a FEI Sirion HR-SEM with a through-the-lens detector (TLD), operated at an acceleration voltage of 10 kV.

Fluorescence Microscopy. Fluorescence microscopy images were acquired in air on an Olympus inverted research microscope IX71 equipped with a mercury burner U-RFL-T as light source and a digital Olympus DP70 camera. Blue excitation ($\lambda_{ex} = 490-510$ nm) and green emission ($\lambda_{em} = 520-550$ nm) were filtered using a Chroma filter cube. Intensity profiles were obtained by averaging the images from three different places at the surface.

X-ray Photoelectron Spectroscopy. XPS measurements were performed on a Physical Electronics Quantera SXM setup equipped with an Al Kα X-ray source (1486.6 eV). A detector angle of 45° was

used, and collected spectra were calibrated on the C 1s peak at 284.8 eV.

■ ASSOCIATED CONTENT

Ⓢ Supporting Information

The Supporting Information is available free of charge on the ACS Publications website at DOI: 10.1021/acsami.6b12997.

    HR-SEM image of silicon micropillars and XPS C 1s spectrum after click chemistry (PDF)

■ AUTHOR INFORMATION

Corresponding Author

*E-mail: j.huskens@utwente.nl.

ORCID Ⓘ

Janneke Veerbeek: 0000-0002-0824-2923
Jurriaan Huskens: 0000-0002-4596-9179

Author Contributions

The manuscript was written through contributions of all authors. All authors have given approval to the final version of the manuscript.

Notes

The authors declare no competing financial interest.

■ ACKNOWLEDGMENTS

■ REFERENCES

(1) Kelzenberg, M. D.; Turner-Evans, D. B.; Putnam, M. C.; Boettcher, S. W.; Briggs, R. M.; Baek, J. Y.; Lewis, N. S.; Atwater, H. A. High-Performance Si Microwire Photovoltaics. *Energy Environ. Sci.* **2011**, *4*, 866−871.

(2) Garnett, E.; Yang, P. D. Light Trapping in Silicon Nanowire Solar Cells. *Nano Lett.* **2010**, *10*, 1082−1087.

(3) Saga, T. Advances in Crystalline Silicon Solar Cell Technology for Industrial Mass Production. *NPG Asia Mater.* **2010**, *2*, 96−102.

(4) Walter, M. G.; Warren, E. L.; McKone, J. R.; Boettcher, S. W.; Mi, Q. X.; Santori, E. A.; Lewis, N. S. Solar Water Splitting Cells. *Chem. Rev.* **2010**, *110*, 6446−6473.

(5) Sun, K.; Shen, S.; Liang, Y.; Burrows, P. E.; Mao, S. S.; Wang, D. Enabling Silicon for Solar-Fuel Production. *Chem. Rev.* **2014**, *114*, 8662−8719.

(6) Edwards, P. P.; Kuznetsov, V. L.; David, W. I. F.; Brandon, N. P. Hydrogen and Fuel Cells: Towards a Sustainable Energy Future. *Energy Policy* **2008**, *36*, 4356−4362.

(7) Nowotny, J.; Sorrell, C. C.; Sheppard, L. R.; Bak, T. Solar-Hydrogen: Environmentally Safe Fuel for the Future. *Int. J. Hydrogen Energy* **2005**, *30*, 521−544.

(8) Tu, W. G.; Zhou, Y.; Zou, Z. G. Photocatalytic Conversion of CO_2 into Renewable Hydrocarbon Fuels: State-of-the-Art Accomplishment, Challenges, and Prospects. *Adv. Mater.* **2014**, *26*, 4607−4626.

(9) Spurgeon, J. M.; Walter, M. G.; Zhou, J. F.; Kohl, P. A.; Lewis, N. S. Electrical Conductivity, Ionic Conductivity, Optical Absorption, and Gas Separation Properties of Ionically Conductive Polymer Membranes Embedded with Si Microwire Arrays. *Energy Environ. Sci.* **2011**, *4*, 1772−1780.

(10) Hou, Y. D.; Abrams, B. L.; Vesborg, P. C. K.; Bjorketun, M. E.; Herbst, K.; Bech, L.; Setti, A. M.; Damsgaard, C. D.; Pedersen, T.; Hansen, O.; Rossmeisl, J.; Dahl, S.; Norskov, J. K.; Chorkendorff, I. Bioinspired Molecular Co-Catalysts Bonded to a Silicon Photocathode for Solar Hydrogen Evolution. *Nat. Mater.* **2011**, *10*, 434−438.

(11) Elbersen, R.; Vijselaar, W.; Tiggelaar, R. M.; Gardeniers, H.; Huskens, J. Effects of Pillar Height and Junction Depth on the Performance of Radially Doped Silicon Pillar Arrays for Solar Energy Applications. *Adv. Energy Mater.* **2016**, *6*, 1501728.

(12) Li, Y. L.; Chen, Q.; He, D. Y.; Li, J. S. Radial Junction Si Micro/Nano-Wire Array Photovoltaics: Recent Progress from Theoretical Investigation to Experimental Realization. *Nano Energy* **2014**, *7*, 10−24.

(13) Kelzenberg, M. D.; Boettcher, S. W.; Petykiewicz, J. A.; Turner-Evans, D. B.; Putnam, M. C.; Warren, E. L.; Spurgeon, J. M.; Briggs, R. M.; Lewis, N. S.; Atwater, H. A. Enhanced Absorption and Carrier Collection in Si Wire Arrays for Photovoltaic Applications. *Nat. Mater.* **2010**, *9*, 239−244.

(14) Fernandez-Serra, M. V.; Adessi, C.; Blase, X. Conductance, Surface Traps, and Passivation in Doped Silicon Nanowires. *Nano Lett.* **2006**, *6*, 2674−2678.

(15) Aberle, A. G. Surface Passivation of Crystalline Silicon Solar Cells: A Review. *Prog. Photovoltaics* **2000**, *8*, 473−487.

(16) Mallorqui, A. D.; Alarcon-Llado, E.; Mundet, I. C.; Kiani, A.; Demaurex, B.; De Wolf, S.; Menzel, A.; Zacharias, M.; Morral, A. I. Field-Effect Passivation on Silicon Nanowire Solar Cells. *Nano Res.* **2015**, *8*, 673−681.

(17) Rahman, M. Z. Advances in Surface Passivation and Emitter Optimization Techniques of C-Si Solar Cells. *Renewable Sustainable Energy Rev.* **2014**, *30*, 734−742.

(18) Qu, Y. Q.; Liao, L.; Cheng, R.; Wang, Y.; Lin, Y. C.; Huang, Y.; Duan, X. F. Rational Design and Synthesis of Freestanding Photoelectric Nanodevices as Highly Efficient Photocatalysts. *Nano Lett.* **2010**, *10*, 1941−1949.

(19) Oh, I.; Kye, J.; Hwang, S. Enhanced Photoelectrochemical Hydrogen Production from Silicon Nanowire Array Photocathode. *Nano Lett.* **2012**, *12*, 298−302.

(20) Reece, S. Y.; Hamel, J. A.; Sung, K.; Jarvi, T. D.; Esswein, A. J.; Pijpers, J. J. H.; Nocera, D. G. Wireless Solar Water Splitting Using Silicon-Based Semiconductors and Earth-Abundant Catalysts. *Science* **2011**, *334*, 645−648.

(21) Warren, E. L.; McKone, J. R.; Atwater, H. A.; Gray, H. B.; Lewis, N. S. Hydrogen-Evolution Characteristics of Ni-Mo-Coated, Radial Junction, n⁺p-Silicon Microwire Array Photocathodes. *Energy Environ. Sci.* **2012**, *5*, 9653−9661.

(22) Ray, N. A.; Van Duyne, R. P.; Stair, P. C. Synthesis Strategy for Protected Metal Nanoparticles. *J. Phys. Chem. C* **2012**, *116*, 7748−7756.

(23) Nemanick, E. J.; Hurley, P. T.; Webb, L. J.; Knapp, D. W.; Michalak, D. J.; Brunschwig, B. S.; Lewis, N. S. Chemical and Electrical Passivation of Single-Crystal Silicon(100) Surfaces through a Two-Step Chlorination/Alkylation Process. *J. Phys. Chem. B* **2006**, *110*, 14770−14778.

(24) O'Leary, L. E.; Johansson, E.; Brunschwig, B. S.; Lewis, N. S. Synthesis and Characterization of Mixed Methyl/Allyl Monolayers on Si(111). *J. Phys. Chem. B* **2010**, *114*, 14298−14302.

(25) Sieval, A. B.; Huisman, C. L.; Schonecker, A.; Schuurmans, F. M.; van der Heide, A. S. H.; Goossens, A.; Sinke, W. C.; Zuilhof, H.; Sudholter, E. J. R. Silicon Surface Passivation by Organic Monolayers: Minority Charge Carrier Lifetime Measurements and Kelvin Probe Investigations. *J. Phys. Chem. B* **2003**, *107*, 6846−6852.

(26) Bashouti, M. Y.; Ristein, J.; Haick, H.; Christiansen, S. A Non-Oxidative Approach Towards Hybrid Silicon Nanowire-Based Solar Cell Heterojunctions. *Hybrid Mater.* **2014**, *1*, 2−14.

(27) Zhang, F. T.; Liu, D.; Zhang, Y. F.; Wei, H. X.; Song, T.; Sun, B. Q. Methyl/Allyl Monolayer on Silicon: Efficient Surface Passivation for Silicon-Conjugated Polymer Hybrid Solar Cell. *ACS Appl. Mater. Interfaces* **2013**, *5*, 4678−4684.

(28) Assad, O.; Puniredd, S. R.; Stelzner, T.; Christiansen, S.; Haick, H. Stable Scaffolds for Reacting Si Nanowires with Further Organic Functionalities While Preserving Si-C Passivation of Surface Sites. *J. Am. Chem. Soc.* **2008**, *130*, 17670−17671.

(29) Ciampi, S.; Eggers, P. K.; Le Saux, G.; James, M.; Harper, J. B.; Gooding, J. J. Silicon (100) Electrodes Resistant to Oxidation in Aqueous Solutions: An Unexpected Benefit of Surface Acetylene Moieties. *Langmuir* **2009**, *25*, 2530−2539.

(30) Plass, K. E.; Liu, X. L.; Brunschwig, B. S.; Lewis, N. S. Passivation and Secondary Functionalization of Allyl-Terminated Si(111) Surfaces. *Chem. Mater.* **2008**, *20*, 2228−2233.

(31) Sieval, A. B.; Linke, R.; Zuilhof, H.; Sudholter, E. J. R. High-Quality Alkyl Monolayers on Silicon Surfaces. *Adv. Mater.* **2000**, *12*, 1457−1460.

(32) Buriak, J. M. Organometallic Chemistry on Silicon Surfaces: Formation of Functional Monolayers Bound through Si-C Bonds. *Chem. Commun.* **1999**, 1051−1060.

(33) Ciampi, S.; Bocking, T.; Kilian, K. A.; James, M.; Harper, J. B.; Gooding, J. J. Functionalization of Acetylene-Terminated Monolayers on Si(100) Surfaces: A Click Chemistry Approach. *Langmuir* **2007**, *23*, 9320−9329.

(34) Elbersen, R.; Tiggelaar, R. M.; Milbrat, A.; Mul, G.; Gardeniers, H.; Huskens, J. Controlled Doping Methods for Radial p/n Junctions in Silicon. *Adv. Energy Mater.* **2015**, *5*, 1401745.

(35) Scheres, L.; Giesbers, M.; Zuilhof, H. Self-Assembly of Organic Monolayers onto Hydrogen-Terminated Silicon: 1-Alkynes Are Better Than 1-Alkenes. *Langmuir* **2010**, *26*, 10924−10929.

(36) Sun, Q. Y.; de Smet, L. C. P. M.; van Lagen, B.; Giesbers, M.; Thune, P. C.; van Engelenburg, J.; de Wolf, F. A.; Zuilhof, H.; Sudholter, E. J. R. Covalently Attached Monolayers on Crystalline Hydrogen-Terminated Silicon: Extremely Mild Attachment by Visible Light. *J. Am. Chem. Soc.* **2005**, *127*, 2514−2523.

(37) Zielke, D.; Petermann, J. H.; Werner, F.; Veith, B.; Brendel, R.; Schmidt, J. Contact Passivation in Silicon Solar Cells Using Atomic-Layer-Deposited Aluminum Oxide Layers. *Phys. Status Solidi RRL* **2011**, *5*, 298−300.

(38) Banerjee, S.; Anderson, W. A. Temperature-Dependence of Shunt Resistance in Photovoltaic Devices. *Appl. Phys. Lett.* **1986**, *49*, 38−40.

(39) Breitenstein, O.; Bauer, J.; Lotnyk, A.; Wagner, J. M. Defect Induced Non-Ideal Dark I-V Characteristics of Solar Cells. *Superlattices Microstruct.* **2009**, *45*, 182−189.

(40) Pudasaini, P. R.; Elam, D.; Ayon, A. A. Aluminum Oxide Passivated Radial Junction Sub-Micrometre Pillar Array Textured Silicon Solar Cells. *J. Phys. D: Appl. Phys.* **2013**, *46*, 235104.

(41) Jansen, H. V.; de Boer, M. J.; Unnikrishnan, S.; Louwerse, M. C.; Elwenspoek, M. C. Black Silicon Method X: A Review on High Speed and Selective Plasma Etching of Silicon with Profile Control: An in-Depth Comparison between Bosch and Cryostat DRIE Processes as a Roadmap to Next Generation Equipment. *J. Micromech. Microeng.* **2009**, *19*, 033001.

(42) Bhairamadgi, N. S.; Gangarapu, S.; Caipa Campos, M. A.; Paulusse, J. M. J.; van Rijn, C. J. M.; Zuilhof, H. Efficient Functionalization of Oxide-Free Silicon(111) Surfaces: Thiol-yne Versus Thiol-ene Click Chemistry. *Langmuir* **2013**, *29*, 4535−4542.

(43) James, M.; Darwish, T. A.; Ciampi, S.; Sylvester, S. O.; Zhang, Z. M.; Ng, A.; Gooding, J. J.; Hanley, T. L. Nanoscale Condensation of Water on Self-Assembled Monolayers. *Soft Matter* **2011**, *7*, 5309−5318.

(44) Salomon, A.; Bocking, T.; Gooding, J.; Cahen, D. How Important Is the Interfacial Chemical Bond for Electron Transport through Alkyl Chain Monolayers? *Nano Lett.* **2006**, *6*, 2873−2876.

(45) Vilan, A.; Yaffe, O.; Biller, A.; Salomon, A.; Kahn, A.; Cahen, D. Molecules on Si: Electronics with Chemistry. *Adv. Mater.* **2010**, *22*, 140−159.

(46) Marrani, A. G.; Cattaruzza, F.; Decker, F.; Zanoni, R.; Cossi, M.; Iozzi, M. F. Molecular and Electronic Properties Transferred to Silicon Via Wet-Chemistry Surface Nanofunctionalization: Ethynylferrocene on Si(100). *J. Nanosci. Nanotechnol.* **2010**, *10*, 2901−2907.

(47) Fabre, B. Functionalization of Oxide-Free Silicon Surfaces with Redox-Active Assemblies. *Chem. Rev.* **2016**, *116*, 4808−4849.

(48) Wold, D. J.; Haag, R.; Rampi, M. A.; Frisbie, C. D. Distance Dependence of Electron Tunneling through Self-Assembled Monolayers Measured by Conducting Probe Atomic Force Microscopy: Unsaturated Versus Saturated Molecular Junctions. *J. Phys. Chem. B* **2002**, *106*, 2813−2816.

(49) Yip, H. L.; Hau, S. K.; Baek, N. S.; Ma, H.; Jen, A. K. Y. Polymer Solar Cells That Use Self-Assembled-Monolayer-Modified ZnO/Metals as Cathodes. *Adv. Mater.* **2008**, *20*, 2376−2382.

(50) Chan, T. R.; Hilgraf, R.; Sharpless, K. B.; Fokin, V. V. Polytriazoles as Copper(I)-Stabilizing Ligands in Catalysis. *Org. Lett.* **2004**, *6*, 2853−2855.